NANO · MICRO small
www.small-journal.com

Hybrid PbS Quantum-Dot-in-Perovskite for High-Efficiency Perovskite Solar Cell

Jianhua Han, Songping Luo, Xuewen Yin, Yu Zhou, Hui Nan, Jianbao Li, Xin Li, Dan Oron, Heping Shen,* and Hong Lin**

In this study, a facile and effective approach to synthesize high-quality perovskite-quantum dots (QDs) hybrid film is demonstrated, which dramatically improves the photovoltaic performance of a perovskite solar cell (PSC). Adding PbS QDs into $CH_3NH_3PbI_3$ ($MAPbI_3$) precursor to form a QD-in-perovskite structure is found to be beneficial for the crystallization of perovskite, revealed by enlarged grain size, reduced fragmentized grains, enhanced characteristic peak intensity, and large percentage of (220) plane in X-ray diffraction patterns. The hybrid film also shows higher carrier mobility, as evidenced by Hall Effect measurement. By taking all these advantages, the PSC based on $MAPbI_3$-PbS hybrid film leads to an improvement in power conversion efficiency by 14% compared to that based on pure perovskite, primarily ascribed to higher current density and fill factor (FF). Ultimately, an efficiency reaching up to 18.6% and a FF of over ≈0.77 are achieved based on the PSC with hybrid film. Such a simple hybridizing technique opens up a promising method to improve the performance of PSCs, and has strong potential to be applied to prepare other hybrid composite materials.

1. Introduction

Organic–inorganic metal halide perovskite solar cells (PSCs) have been extensively developed in the last few years with the power conversion efficiency (PCE) reaching a certified value of 22.7%.[1,2] Perovskite materials show strong promise to work as efficient photovoltaic absorbers, owing to their extraordinary optoelectronic properties including strong light absorption, ambipolar carrier transport character, easy fabrication, long diffusion length, and high mobility.[3–6] Developing high-quality perovskite films is of paramount importance to further push the perovskite solar cell efficiency to a regime of over 25%. A variety of approaches including solvent engineering,[7] compositional engineering,[8] and interface engineering are viable to improve the perovskite layer quality.[9,10] For one, we have recently shown that introducing photoactive semiconductor nanoparticles or quantum dots (QDs) in the perovskite material can serve as an effective means to improve the perovskite layer quality and its optoelectronic property by providing controlled nucleation sites which can lead to crystalline growth along preferred orientations.[11] QDs themselves also display advantageous properties, including high absorption coefficient, tunable bandgap by controlling the nanoparticle diameter, low cost, and solution processability.[12,13] On the other hand, the most efficient PSCs reported so far are based on lead (Pb)–iodine perovskite with a bandgap of ≈1.6 eV,[8] such that performance enhancement can be expected by redshifting the absorption edge of the device.[14] Exploiting lower bandgap perovskites still lags behind, and the most successful candidate to date is based on a Sn/Pb binary perovskite which is notorious for instability issues.[15] Employing hybrid perovskite–QDs can adequately address this issue, as it renders possibilities to broaden the light response range and ultimately realize widened spectrum absorption by employing narrower bandgap QDs.[11,16] There are a variety of QD candidates that have strong response in the near-infrared spectrum region, including PbS,[17] Ag_2S,[18] and SnS.[19] PbS QDs have been developed as one of the most efficient absorbers, beyond the

J. H. Han, S. P. Luo, X. W. Yin, Y. Zhou, H. Nan, Prof. J. B. Li, Prof. H. Lin
State Key Laboratory of New Ceramics and Fine Processing
School of Materials Science and Engineering
Tsinghua University
Beijing 100084, China
E-mail: hong-lin@tsinghua.edu.cn
Prof. J. B. Li
State Key Laboratory of Marine Resource Utilization in South China Sea
Materials and Chemical Engineering Institute
Hainan University
Haikou 570228, China
The ORCID identification number(s) for the author(s) of this article can be found under https://doi.org/10.1002/smll.201801016.

DOI: 10.1002/smll.201801016

Prof. X. Li
Pen-Tung Sah Institute of Micro-Nano Science and Technology
Xiamen University
Xiamen 361000, China
Prof. D. Oron
Department of Physics of Complex Systems
Weizmann Institute of Science
Rehovot 76100, Israel
E-mail: dan.oron@weizmann.ac.il
Dr. H. P. Shen
Centre for Sustainable Energy System
Research School of Engineering
Australian National University
Canberra 2601, Australia
E-mail: heping.shen@anu.edu.au

advantages including earth-abundant elements, solution processability, and multiple exciton generation effect.[20–22] More importantly, the PbS lattice matches well with the perovskite structure, as both $MAPbI_3$ and PbS possess a six-coordinated Pb atom, and with Pb—Pb distances ($MAPbI_3$, 6.26 Å; PbS, 5.97 Å) that are within 4.6% of one another.[23] Perovskite–PbS QD hybrid films have been previously applied in solar cells using a core–shell structure, albeit with an efficiency that is still not satisfactory. Seok and co-workers reported PbS QD/$MAPbI_3$ core/shell material–based solar cells and achieved an efficiency of only 3.2%.[24] Liang and co-workers fabricated solar cells based on PbS quantum dot capped with $MAPbI_3$ and achieved the best PCE of 5.28% using a structure of F-doped SnO_2 (FTO)/TiO_2/$MAPbI_3$–PbS/MoO_x/Au.[21] As an alternative for construction of the device from nanoparticles, conversion of a mixed solution phase into a solid phase shows significant promise, as it significantly broadens the range of realizable designs. This can potentially enable functionalities that are not attainable in the single-phase constituents. This kind of hybrid material, namely quantum-dot-in-matrix, was first synthesized by Ning et al. employing an epitaxial growth process coupled with a two-step perovskite preparation technique.[23] Despite deep investigation into the physical properties of this hybrid material, no application in solar cells has, to date, been demonstrated. Moreover, the two-step method employed to fabricate the perovskite material is significantly more complicated than its one-step counterpart, such that it is hard to precisely control the stoichiometry of the resultant perovskite material.[25]

Here, we developed a one-step method to prepare the $MAPbI_3$–PbS QD hybrid precursor with preformed QDs homogeneously dispersed in $MAPbI_3$ layer, and to directly grow it on a mesoporous-TiO_2 (mp-TiO_2) substrate via an in situ crystallization process. In detail, both $MAPbI_3$ and PbS QDs were dispersed in the same solvent mixture of *N*,*N*-dimethylformamide (DMF) and dimethylsulfoxide (DMSO) in advance, enabling easy mixing for any desired ratio. Such a hybrid material can not only retain the advantageous properties of both perovskite and QDs (including optical and electrical properties), but can potentially have the capability to extend the absorption range of the device. Moreover, it is found that adding a small amount of PbS QDs significantly improved the crystallinity of perovskite by supplying extra nucleation sites, with an extremely low lattice mismatch (≈1%) of the interplanar spacing between $MAPbI_3$ and PbS. Correspondingly, we achieved an efficiency of 18.6% for the solar cell based on $MAPbI_3$–PbS QD hybrid film, resulting in an improvement by 14.1% compared with those based on the pure $MAPI_3$ films. Besides the better crystalline properties of perovskite (larger crystal grain size, better morphology, higher crystallinity) and marginally broadened light absorption region in $MAPbI_3$/PbS QD hybrid films, the carrier mobility was also enhanced prominently, which is beneficial for improving the charge collection.

2. Results and Discussion

This work employs a facile $MAPbI_3$–QD hybridizing technique to fabricate a "dots-in-a-matrix" crystals that take advantage of the best features of each, thus showing outstanding optoelectronic properties. Both perovskite and PbS QDs were dissolved or dispersed in the DMF/DMSO mixture solution separately, and a simple mixing of the two can result in a hybrid solution at any required concentration and ratio. As shown in Figure S1 (Supporting Information), the $MAPbI_3$–PbS QD hybrid solution looks clear while browner than the pure $MAPbI_3$ solution, indicating that PbS QDs have been successfully solubilized in the $MAPbI_3$ solution. Such a uniformly dispersed solution is vital for producing a homogeneous and high-quality film with few defects and little disorder.

The benefit of constructing the perovskite/PbS QD hybrid film for improving the photovoltaic performance of the as-prepared solar cells is first demonstrated. We used a standard n–i–p device structure in this work, which is composed of FTO/cp-TiO_2/mp-TiO_2/perovskite layer/*N*,*N*-di(4-methoxyphenyl)amino]-9,9′-spirobifluorene (spiro-OMeTAD)/Au (cp-TiO_2 represents compact TiO_2 layer). The *J*–*V* curves of the devices without and with different concentrations of PbS QDs are shown in **Figure 1**A, with the detailed photovoltaic parameters given in **Table 1**. We found that solar cells based on the $MAPbI_3$–PbS QD hybrid films show apparently higher short-circuit current density (J_{sc}) and fill factor (FF), as shown in Figure 1B,C. The pure perovskite solar cell shows an average J_{sc} of 21.9 mA cm^{-2}, while 0.2 mg mL^{-1} PbS doping increased the J_{sc} to 22.4 mA cm^{-2} and 0.5 mg mL^{-1} further raised it to 23.5 mA cm^{-2}. However, too much PbS QDs seems to be detrimental for the device performance, as the current dropped to 22.0 mA cm^{-2}. Surprisingly, we also observe a significantly enhanced FF for the perovskite–PbS QD hybrid solar cell, reaching up to ≈0.77 compared to ≈0.73 for the device based on pure perovskite film. The FF obtained by the perovskite–PbS QD film was among the highest reported values for the standard mesoporous structured perovskite solar cells.[26–28] The V_{oc} of PSCs based on $MAPbI_3$–PbS QD hybrid films is nearly unchanged compared to that based on the pure $MAPbI_3$. Eventually, the device based on the $MAPbI_3$–PbS QDs (0.5 mg mL^{-1}) hybrid film displayed a champion PCE of 18.6%, resulting in an increment by ≈14% compared with 16.3% for the pristine solar cells. To elucidate the origin of such prominent improvement in photovoltaic performance, especially the increase in FF, we then moved to deeply study the crystalline properties and optoelectronic properties of such a perovskite–PbS QD hybrid film.

Consistent with the observation for the device performance, adding PbS QDs in the perovskite precursor solution is found to be beneficial for the perovskite crystallization, as investigated by X-ray diffraction (XRD) (**Figure 2**). Both the perovskite films without and with PbS additive show diffraction peaks at 14.2°, 28.5°, and 31.9°, corresponding to (110), (220), and (330) of the tetragonal $MAPbI_3$ phase, respectively.[29] Nevertheless, the three strongest peaks corresponding to (110), (220), and (330) planes were significantly enhanced for the $MAPbI_3$–PbS QD hybrid films, indicating improved crystalline properties of $MAPbI_3$. Furthermore, the intensity ratio of (220) versus (110) was also increased when hybridizing the $MAPbI_3$ with PbS QDs, which would impose a positive effect on the device performance as the former has been reported to be

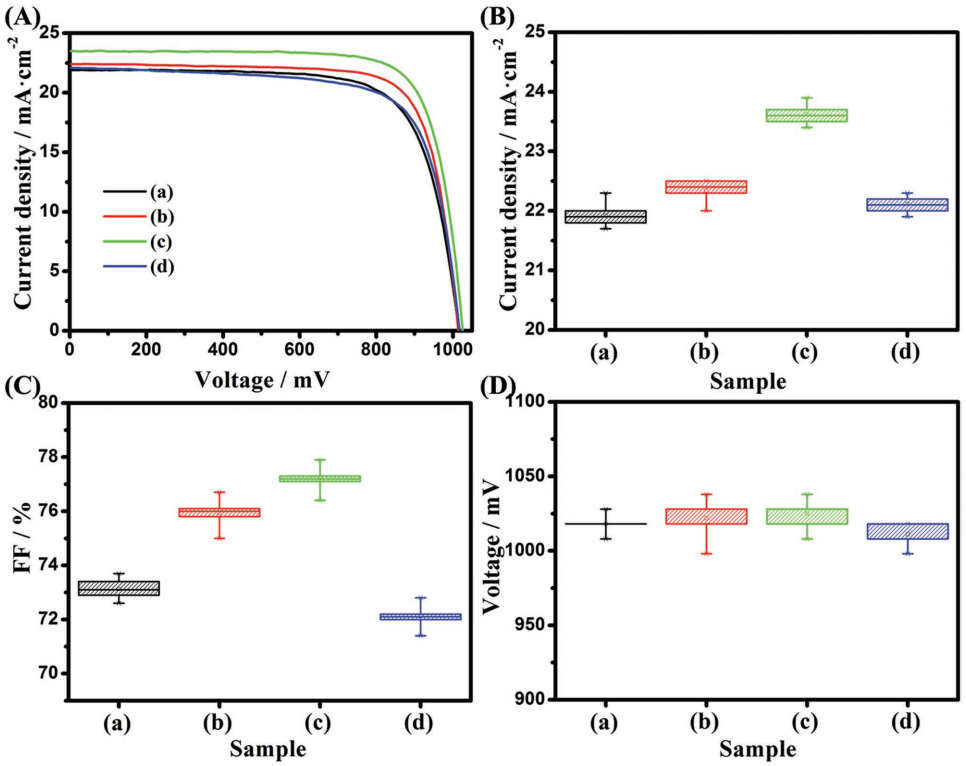

Figure 1. A) *J–V* curves, box-line graphs of B) J_{sc}, C) FF, and D) V_{oc} of SCs based on a) $MAPbI_3$ films, $MAPbI_3$–PbS QD hybrid films with PbS concentration of b) 0.2 mg mL^{-1}, c) 0.5 mg mL^{-1}, and d) 1 mg mL^{-1}.

beneficial for hindering the bulk carrier recombination.[30,31] Adding too much PbS QDs in the perovskite solution tends to become detrimental for the crystallization of the perovskite, as undesirable peaks appeared and the weaker strongest peak than other MAPI–PbS hybrid films in the XRD pattern (Figure 2D). The poor crystalline properties of the as-prepared films could deteriorate the charge transport process, thus contributing as a primary cause for the current drop of the as-prepared device. The weak peak at $2\theta = 30.07°$ in Figure 2D is the (200) plane of PbS in rock-salt crystalline structure (PDF#05-0592), which is not observable when the PbS amount added in the precursor is small (Figure 2B,C). Meanwhile, PbI_2 peak (12.67°, PDF#07-0235) appears in Figure 2D, indicating that excess PbS QDs in precursor solution results in incomplete reaction between PbI_2 and methylammonium iodide (MAI) even though he molar ratio of these two precursors is 1:1.

Table 1. Photovoltaic parameters derived from *J–V* measurement of cells based on different absorber layers.

Sample	η [%]	V_{oc} [mV]	J_{sc} [mA cm^{-2}]	FF [%]	R_s [Ω cm^2]	R_{sh} [× 10^4 Ω cm^2]
Pure $MAPbI_3$	16.3	1018	21.9	73.1	4.20	1.18
0.2 mg mL^{-1} QDs–$MAPbI_3$	17.5	1028	22.4	76.0	3.27	2.18
0.5 mg mL^{-1} QDs–$MAPbI_3$	18.6	1028	23.5	77.2	2.78	2.34
1 mg mL^{-1} QDs–$MAPbI_3$	16.2	1018	22.1	72.0	3.57	1.06

As a key factor for the photovoltaic performance of the solar cells, the light absorption property of the perovskite absorber layer was then characterized by the UV–vis spectrophotometer (**Figure 3**A). As anticipated, $MAPbI_3$–PbS QD hybrid films demonstrate a small increase of the absorption in the visible spectrum range, and an extended absorption

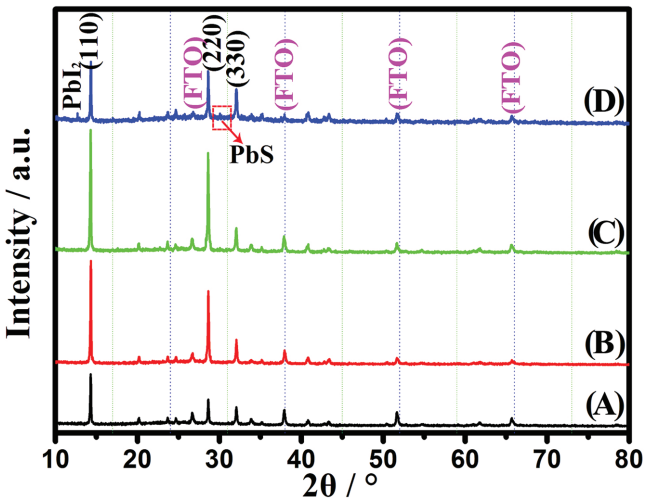

Figure 2. XRD patterns of A) $MAPbI_3$ films, $MAPbI_3$–PbS QDs with PbS concentration of B) 0.2 mg mL^{-1}, C) 0.5 mg mL^{-1}, and D) 1 mg mL^{-1}.

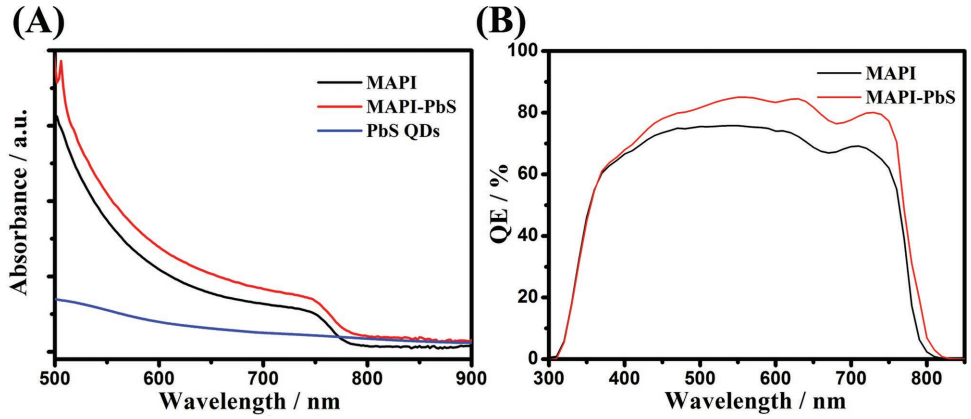

Figure 3. A) Absorbance spectra and B) quantum efficiency spectra of the as-prepared samples.

to the near-infrared to 900 nm compared to that of the pure $MAPbI_3$ film. The increased absorption in the near-infrared is probably due to narrower bandgap of PbS QDs and the shift of the band-edge due to the small strain at the QD–$MAPI_3$ interface.[32–34] Some broadening of the optical response toward the red is also observed in the incident photon-to-current efficiency (IPCE) spectra in Figure 3B. It can be seen that slight mismatch between integrated J in IPCE and J_{sc} in J–V curves occurred. This phenomenon can be attributed to the small J–V hysteresis behavior existing in our device. J–V measurement with both reverse and forward scanning mode and maximum power point tracking results are displayed in Figure S2 (Supporting Information). The current densities in both J–V measurement with forward scanning mode and maximum power point tracking results are lower than that in J–V measurement with reverse scanning mode. All the results show that the hysteresis leads to the integrated J in IPCE mismatching with the J_{sc} in J–V measurement. This also partially contributes to the smaller integrated current density from IPCE than that from the J–V measurement, although the discrepancy between these two has been extensively reported even in hysteresis-less devices (usually IPCE integrated current smaller than that extracted from IV scanning).[35–37] Notably, however, it appears that wavelengths beyond ≈820 nm due to the reduced bandgap of $MAPI_3$–PbS QD films, do not contribute significantly to the current. Rather, we find that the increased current yield of the perovskite–PbS hybrid film primarily originates from the enhanced response in the range of 400–800 nm. This further indicates that the changes induced by the presence of PbS QDs to the crystalline properties of perovskite in the hybrid film are those which appear to improve the charge transport and collection efficiency. This, correspondingly, could be a major contributor to the extraordinary FF for the device based on $MAPbI_3$/PbS hybrid film in this work.

The charge transport and separation properties of the photogenerated carriers of pure $MAPbI_3$ films and $MAPbI_3$–PbS QD hybrid films were then investigated by steady photoluminescence (PL) (**Figure 4**A) and time-resolved PL (TRPL) measurement (Figure 4B). We note that all the perovskite films were deposited on the FTO/cp-TiO_2 layer/mp-TiO_2 layer substrate to mimic the conditions in the solar cell. $MAPbI_3$–PbS QD hybrid films show reduced PL intensity, indicating more efficient charge transfer process than pure $MAPbI_3$ film.[21] Accompanied with this is a PL peak redshift, indicating that the hybrid film can absorb and utilize more incident light than the pure $MAPbI_3$ film. Figure 4B,C displays the TRPL measurements of the as-prepared FTO/electron transport layer (ETL)/MAPI(–PbS) and FTO/ETL/MAPI(–PbS)/hole transport layer (HTL), respectively, it can be seen the carrier extraction process was accelerated in the as-prepared films with HTL. As shown in Figure 4B,C, the extracted lifetimes from these two conditions are much shorter compared to that of the $MAPbI_3$ pure film. Therefore, the electrons and holes can be separated and transported more efficiently, which is beneficial for suppressing the charge recombination. The electrochemical impedance response of the devices was then measured under dark condition (Figure 4D shows the Nyquist spectra), which supplies information about the charge transport between the carrier selective layer and perovskite layer.[5,38] The device based on the hybrid film shows an arc with a smaller radius, indicating larger charge transport efficiency. Consistent with the variation of series resistance (R_s) and shunt resistance (R_{sh}) in Table 1, lower value of R_s indicates better transport performance. $MAPbI_3$–PbS QDs formed a bulk heterojunction in hybrid structure where the PbS QDs were distributed in the $MAPbI_3$ layer, which is beneficial for carrier transport.[39] The results of PL and electrochemical impedance spectra testify that the properties of carrier separation and transport can be improved by hybridizing the $MAPbI_3$ with PbS QDs.

The top surface of $MAPbI_3$ and $MAPbI_3$–PbS QD hybrid films and the cross-sectional morphology of the as-prepared solar cells are shown in **Figure 5**. The $MAPbI_3$–PbS hybrid films show larger grain size than that of pure $MAPbI_3$ films, coupled with fewer fragmental grains. We think that the PbS QDs supply nucleation sites in the hybrid precursor solution that promote the perovskite nucleation and allow them to grow into larger crystalline grains. Large perovskite grains can promote carrier transport in the absorber layer due to the low amount of defect and trap states in crystalline structure.[40,41] Meanwhile, such better crystallinity properties of perovskite–PbS QD hybrid film compared to the pure perovskite film can

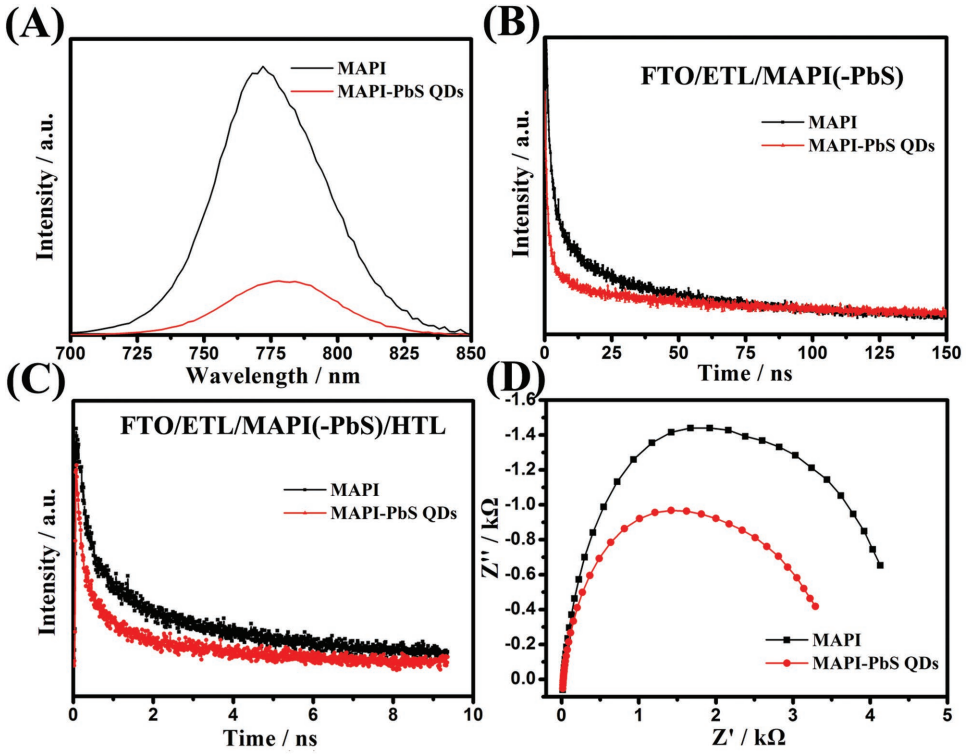

Figure 4. A) Steady-state PL spectra, time-resolved PL spectra with test structure of B) FTO/ETL/MAPI(–PbS), C) FTO/ETL/MAPI(–PbS)/HTL, and D) EIS spectra of the as-prepared samples.

lead to higher carrier separation and transport efficiency in perovskite layer,[29–41] which is consistent with our observations in the photovoltaic performance.

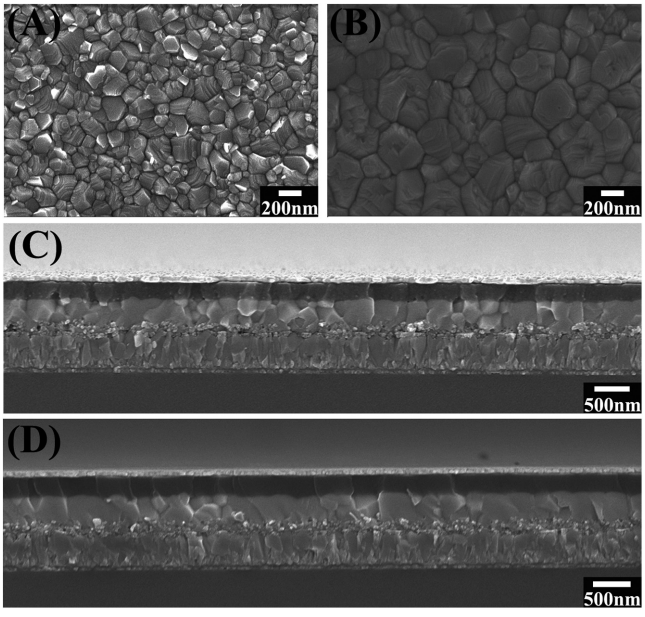

Figure 5. SEM images of A) $MAPbI_3$ and B) $MAPbI_3$–PbS hybrid films. Cross-sectional SEM images of C) $MAPbI_3$ and D) $MAPbI_3$–PbS hybrid films.

The cross-sectional scanning electron microscope (SEM) images of the solar cells based on pure $MAPbI_3$ and $MAPbI_3$–PbS QD hybrid films are displayed in Figure 5C,D, respectively. The compact TiO_2 layer has a thickness of 50 nm, and the thickness of the mp-TiO_2 layer is 150 nm. Pure $MAPbI_3$ or $MAPbI_3$–PbS QD hybrid films (absorber layer) were prepared on the mp-TiO_2 layer with no visible pinholes or cracks. However, the thickness of the $MAPbI_3$–PbS QD hybrid film (≈490–500 nm) is slightly higher than that of the pure perovskite film (≈470–480 nm), which might be due to the larger crystalline grain size of hybrid film.

PbS QDs synthesized in this work are uniform with an average size of ≈4 nm, as revealed by the transmission electron microscopy (TEM) and energy dispersive spectrometer (EDS) images (Figure S3, Supporting Information). From the high-resolution TEM (HRTEM) image, the interplanar spacing of 2.97 Å corresponds to the crystalline lattice (200) of PbS with a rock-salt structure. Inset of Figure S3B (Supporting Information) shows the fast Fourier transformed selected area diffraction pattern (FFT-SAD) of PbS QDs, indicating that the preferred lattice orientation of PbS QDs was (200). Elemental analysis demonstrates the anticipated stoichiometric ratio of 1:1 for Pb:S. The microstructure details of $MAPbI_3$ was achieved by TEM analysis accompanied with the FFT-SAD. Figure S4 (Supporting Information) shows a typical HRTEM image of pure $MAPbI_3$ materials, the lattice spacing of 3.0 Å matches well with the crystalline planar (220) of $MAPbI_3$.[42] The lattice orientation of $MAPbI_3$ in TEM image keeps at almost the same direction, suggesting that the $MAPbI_3$ has an

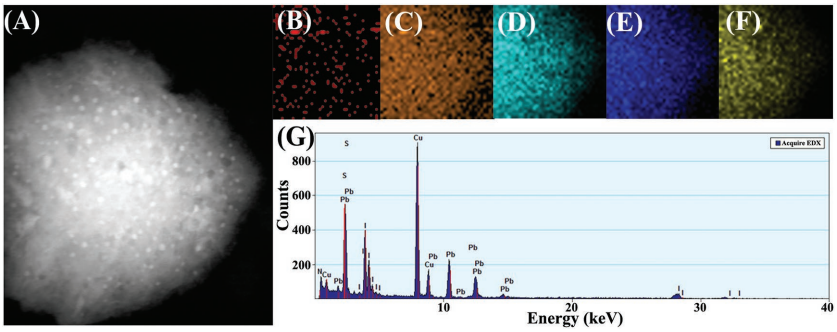

Figure 6. A) TEM image of $MAPbI_3$–PbS hybrid structure. B–F) Elemental distribution mapping of C, N, I, Pb, S in hybrid structure. G) EDS spectrum of $MAPI_3$–PbS hybrid structure.

ideal crystalline structure. The inset in Figure S4 (Supporting Information) shows the FFT-SAD pattern. The strongest signal corresponds to the planar (220) of $MAPbI_3$, consistent with the lattice orientation of $MAPbI_3$ in HRTEM image. Nevertheless, other weak signals also emerged in the inset, which is probably due to the impurity produced from the electron beam irradiation.

In order to investigate the hybrid structure of $MAPbI_3$–PbS QDs, the combinational characterization of TEM and elemental mapping analysis (**Figures 6** and **7**) were performed. TEM image of $MAPbI_3$–PbS hybrid structure with a relatively low magnification (320 000×) is shown in Figure 6A, and the elemental mapping images of C, N, I, Pb, S in hybrid structure are shown in Figure 6B–F, respectively. It is clear that the QDs are distributed homogeneously in the hybrid structure. The distribution states of N, I, Pb, S is similar with that of $MAPbI_3$ and PbS QDs in TEM image, while the signal of C is largely attributed to the carbon films on copper grid. Figure 6G shows the EDS spectrum of $MAPbI_3$–PbS hybrid films, suggesting that the hybrid structure was composed of the elements of N, Pb, I, and S. Meanwhile, the presence of $MAPbI_3$ and PbS in hybrid films was further verified by the X-ray photoelectron spectroscopy (XPS) spectra shown in Figure S5 (Supporting Information). Pb, S, and I were all detected in the as-prepared sample. The binding energy position at 161.2 eV can be assigned to the S element in PbS.[43]

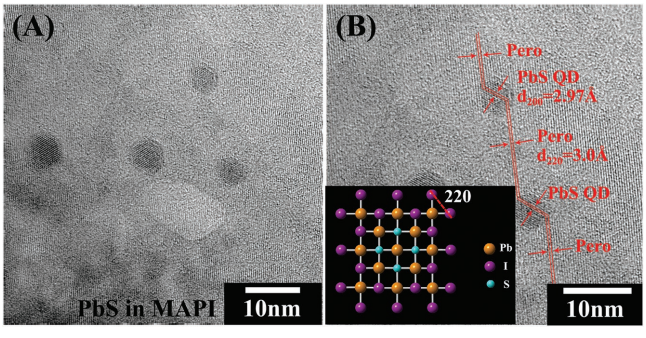

Figure 7. A) HRTEM image and B) large view HRTEM image with marked crystalline lattice of $MAPbI_3$–PbS hybrid structure. Inset shows the molecular schematic of hybrid structure of PbS QDs in $MAPI_3$, lattice 220 of $MAPbI_3$ consists of I^-.

More detailed structure information of the $MAPbI_3$–PbS QD hybrid film was further offered by the HRTEM image (Figure 7). PbS QDs were found to be dispersed and imbedded in the perovskite base structure homogeneously. The crystalline lattice space of 2.97 Å of the small particles was consistent with the PbS QDs in Figure S3 (Supporting Information), thus the particles in hybrid structure are PbS QDs. The interplanar spacing of the background (≈3.0 Å) is consistent with that of the pure $MAPbI_3$ shown in Figure S4 (Supporting Information). Based on these observations, the molecular schematic of interface of hybrid structure was presented in the inset of Figure 7B. I^- ions existing on the crystalline plane (220) in $MAPbI_3$ enable PbS QDs to coordinate with the I^- in the $MAPbI_3$. Finally, the $MAPbI_3$–PbS QD hybrid structure was developed after the PbS QDs coordinate with I^-. In order to investigate the phase distribution in MAPI–PbS QD hybrid films, the UV–vis absorption measurement with the incident light either from both the front and the back sides was performed (Figure S6, Supporting Information). We notice that the absorption spectra from the two directions are almost identical, indicating that the phase segregation or phase gradient is negligible in the dots-in-matrix system fabricated. We therefore conclude that the $MAPI_3$–PbS QD hybrid structure with uniformly distributed QDs in matrix was successfully prepared based on our hybridizing technique.

Hall effect measurement of $MAPbI_3$ and $MAPbI_3$–PbS QD hybrid films on glass substrate was carried out based on a model shown in Figure S7 (Supporting Information), and electrical parameters are summarized in **Table 2**. Embedding PbS QDs in $MAPbI_3$ is found to significantly increase the carrier mobility from 3.779×10^{-3} to 1.173×10^{-1} m^2 V^{-1} s^{-1}. Concurrently, the carrier concentration decreased by almost twice, from 2.888×10^{15} to 1.741×10^{15} m^{-3}. The improved carrier Hall mobility could be derived from better crystalline properties and surface morphology of $MAPbI_3$–PbS QD hybrid films.[44] Higher carrier mobility is beneficial for yielding higher charge collection efficiency,[45,46] thus contributing to a largely increased current density and outstanding FF in the as-prepared solar cells.

Table 2. Hall effect test parameters of $MAPbI_3$ and $MAPbI_3$–PbS hybrid films.

	Samples	$MAPI_3$–PbS	$MAPI_3$
μ_H	Hall mobility [m^2 V^{-1} s^{-1}]	1.173E-1	3.779E-3
n	Carrier concentration [m^{-3}]	1.741E14	2.888E15
n_{sheet}	Sheet carrier concentration [m^{-2}]	3.483E7	5.775E8
R_H	Hall coefficient [m^3 C^{-1}]	3.584E4	2.161E3
R_{Hsheet}	Sheet Hall coefficient [m^2 C^{-1}]	1.792E11	1.081E10
ρ	Resistivity [Ω m]	−3.056E5	−5.720E5
ρ_{sheet}	Sheet resistivity [Ω $\square^{-1}$]	−1.528E12	−2.860E12
V_H	Hall voltage [V]	3.5819E0	−1.8977E-1

3. Conclusion

We report herein a simple one-step method to synthesize high-quality $MAPbI_3$–PbS QD hybrid film, where PbS QDs distribute uniformly in the $MAPbI_3$ crystal structure. The absorption of photons in the near-infrared region of PbS QDs can extend the light absorption of the hybrid film. The $MAPbI_3$–PbS QD hybrid film was then successfully incorporated into a mesoscopic perovskite solar cell, resulting in an impressive PCE of 18.6%, corresponding to an improvement by 14% compared to that based on pure $MAPbI_3$ film. The improvement of the device performance not only lies in the current increase, but the fill factor as well. This is ascribed to the significantly enhanced crystalline properties of $MAPbI_3$ films in the hybrid structure, revealed by enlarged crystalline grain, reduced fragmentized grains, stronger XRD peak intensity, and more content of plane of (220). The hybridizing technique developed in this work can not only serve as a viable routine to further improve the photovoltaic performance of PSCs, but also opens up large opportunity to be incorporated into other high-performance optoelectronic devices due to their extraordinary crystallization property and optoelectronic properties.

4. Experimental Section

Material Synthesis and Device Fabrication: FTO-coated glass substrate (sheet resistance ≈ 7 Ω sq^{-1}, Nippon, Tokyo, Japan) was patterned by etching with a mixture of zinc powder and hydrochloric acid (HCl, 2 M). The substrate was then cleaned with detergent, deionized water, ethanol, acetone, and isopropanol by ultrasonication for 20 min, respectively. They were further treated in ultraviolet/O_3 cleaner for 15 min before the film deposition. Compact TiO_2 layer was deposited on the FTO substrate by spin-coating a precursor solution of titanium isopropoxide at 2000 rpm, and annealed at 500 °C for 0.5 h.[11] Mesoporous TiO_2 layer with a thickness of ≈150 nm was fabricated on the compact layer through spin-coating the diluted TiO_2 paste in ethanol (120 mg mL^{-1}, 30 NR, Dyesol, Australia), followed by drying at 150 °C for 0.5 h and annealing at 500 °C for 1 h.

Colloidal PbS QDs were synthesized according to previous work.[47] In detail, 53 mg sulfur (S) was added in 5 mL oleylamine (OA) with stirring at 120 °C for 0.5 h. Meanwhile, 840 mg lead chloride ($PbCl_2$) was dissolved in 7.5 mL OA in a three-neck flask under nitrogen condition at 125 °C for 0.5 h. Then, 2.25 mL solution of S in OA coupled with 170 µL tri-*n*-octylphosphine (TOP) was injected into the $PbCl_2$ solution. The temperature was lowered down to 80 °C, and maintained at this value for 13 min. The as-prepared dried and washed PbS QDs (0.2, 0.5, 1 mg) were dispersed in 1 mL mixed solvent of DMF and DMSO with a volume ratio of 4:1.

The one-step method was then used to prepare both the pure and the hybrid perovskite film in this work. The pure perovskite precursor solution was composed of 1.35 M MAI (Dyesol) and lead iodide (PbI_2, Aldrich) with a molar ratio of 1:1 in a mixture of DMF and DMSO (volume ratio of 4:1). The $MAPbI_3$–PbS QD hybrid precursor solution was prepared by dissolving the MAI and PbI_2 in the preformed PbS QDs dispersion solution with a molar ratio of 1:1. The $MAPbI_3$ or $MAPbI_3$–PbS QD hybrid films were deposited on the mesoporous TiO_2 layer by spin-coating the precursor solution at 1000 rpm for 10 s, followed by 5000 rpm for 20 s. At the 15 s during the second step, 300 µL chlorobenzene (CB) was dripped on the spinning substrate. The samples were annealed at 100 °C for 20 min in a N_2-filled glove box.

The HTL precursor solution, composed of 60×10^{-3} M spiro-OMeTAD (Borun Chemical Co., Ltd., Zhejiang, China), 17.5 µL bis(trifluoromethane)-sulfonimide lithium salt (LiTFSI) and 4-*tert*-butylpyridine (TBP, 28.8 µL) in CB (1 mL), was spin-coated on the perovskite layer at 4000 rpm for 40 s. To complete the device, a gold top electrode was evaporated on the spiro-OMeTAD layer with thickness of ≈200 nm.

Characterization: The current density–voltage (*J*–*V*) curves were obtained under illumination with a solar simulator (100 mW cm^{-2}, 94043A, Newport, USA) and a Keithley 2400 source meter for carrying out the *I*–*V* scans. XRD patterns were achieved by X-ray diffractometer (D8 Advance, Bruker, Germany) with a Cu-Kα (1.5406 Å) radiation operating at 40 kV. The light absorption properties were tested by the UV–vis spectrophotometer (Lambda 950, Perkin Elmer, USA). The IPCE spectra were obtained by the quantum efficiency system (QEX10, PV measurements, USA), which was calibrated by a standard crystalline silicon solar cell. Steady-state and time-resolved PL spectra were achieved using a fluorescence spectrometer (FLS920, Edinburgh Instruments, UK), which were photoexcited by monochromatic xenon lamp source (central wavelength λ_{exc} = 460 nm) and laser beam with wavelength of 405 nm (EPL405), respectively. Electrochemical impedance spectroscopy (EIS) was characterized using the Zahner system (Zennium Zahner, Germany) in dark condition with a bias of 0.8 V, with the frequency ranging from 1 Hz to 1 MHz and a modulation amplitude of 10 mV. TEM and HRTEM images were conducted on a TEM system at 100 kV (Tecnai G2, FEI Company, USA) equipped with an elemental distribution mapping detector. The SEM image was recorded by field emission scanning electron microscopy at 5 kV (Zeiss LEO-1530, Germany). The Hall effect measurement was carried out using a Lake Shore Hall test system 8400 with type of van der Pauw and excitation field of 5 kG. The sample structure for the Hall effect measurement is shown in Figure S1 (Supporting Information).

Supporting Information

Supporting Information is available from the Wiley Online Library or from the author.

Acknowledgements

This work was financially supported by the Projects of International Cooperation and exchanges NSFC (51561145007), the National Natural Science Foundation of China (51772166), the Sino-Italy International Cooperation on Innovation (2016YFE0104000), the National Energy Novel Materials Center (NENMC–II–1705), and the Israel Science Foundation ISF–NSFC program.

Conflict of Interest

The authors declare no conflict of interest.

Keywords

crystallization, hybridizing technique, PbS, perovskite solar cells, quantum dots

Received: March 15, 2018
Revised: May 15, 2018
Published online:

[1] M. Saliba, T. Matsui, K. Domanski, J. Y. Seo, A. Ummadisingu, S. M. Zakeeruddin, J. P. Correa-Baena, W. R. Tress, A. Abate, A. Hagfeldt, M. Grätzel, *Science* **2016**, *354*, 206.

[2] Best Research-Cell Efficiencies, National Renewable Energy Laboratory, https://www.nrel.gov/pv/assets/images/efficiency-chart.png (accessed: March 2018).
[3] M. He, X. C. Pang, X. Q. Liu, B. B. Jiang, Y. J. He, H. Snaith, Z. Q. Lin, *Angew. Chem., Int. Ed.* **2016**, *55*, 4280.
[4] M. A. Green, A. H. Baillie, H. J. Snaith, *Nat. Photonics* **2014**, *8*, 506.
[5] X. W. Yin, Z. B. Yao, Q. Luo, X. Z. Dai, Y. Zhou, Y. Zhang, Y. Y. Zhou, S. P. Luo, J. B. Li, N. Wang, H. Lin, *ACS Appl. Mater. Interfaces* **2017**, *9*, 2439.
[6] D. P. McMeekin, G. Sadoughi, W. Rehman, G. E. Eperon, M. Saliba, M. T. Hörantner, A. Haghighirad, N. Sakai, L. Korte, B. Rech, M. B. Johnston, L. M. Herz, H. J. Snaith, *Science* **2016**, *351*, 151.
[7] N. J. Jeon, J. H. Noh, Y. C. Kim, W. S. Yang, S. Ryu, S. I. Seok, *Nat. Mater.* **2014**, *13*, 897.
[8] N. J. Jeon, J. H. Noh, W. S. Yang, Y. C. Kim, S. Ryu, J. Seo, S. I. Seok, *Nature* **2015**, *517*, 476.
[9] H. P. Zhou, Q. Chen, G. Li, S. Luo, T. B. Song, H. S. Duan, Z. R. Hong, J. B. You, Y. S. Liu, Y. Yang, *Science* **2014**, *345*, 542.
[10] J. P. C. Baena, L. Steier, W. Tress, M. Saliba, S. Neutzner, T. Matsui, F. Giordano, T. J. Jacobsson, A. R. S. Kandada, S. M. Zakeeruddin, A. Petrozza, A. Abate, M. K. Nazeeruddin, M. Grätzel, A. Hagfeldt, *Energy Environ. Sci.* **2015**, *8*, 2928.
[11] J. H. Han, X. W. Yin, H. Nan, Y. Zhou, Z. B. Yao, J. B. Li, D. Oron, H. Lin, *Small* **2017**, *13*, 1700953.
[12] G. S. Wang, H. Y. Wei, J. J. Shi, Y. Z. Xu, H. J. Wu, Y. H. Luo, D. M. Li, Q. B. Meng, *Nano Energy* **2017**, *35*, 17.
[13] P. V. Kamat, K. Tvrdy, D. R. Baker, J. G. Radich, *Chem. Rev.* **2010**, *110*, 6664.
[14] F. Hao, C. C. Stoumpos, R. P. H. Chang, M. G. Kanatzidis, *J. Am. Chem. Soc.* **2014**, *136*, 8094.
[15] A. Rajagopal, P. W. Liang, C. C. Chueh, Z. B. Yang, A. K. Y. Jen, *ACS Energy Lett.* **2017**, *2*, 2531.
[16] Y. Yang, W. Y. Wang, *J. Power Sources* **2015**, *293*, 577.
[17] N. Zhao, T. P. Osedach, L. Y. Chang, S. M. Geyer, D. Wanger, M. T. Binda, A. C. Arango, M. G. Bawendi, V. Bulovic, *ACS Nano* **2010**, *4*, 3743.
[18] A. Tubtimtae, K. L. Wu, H. Y. Tung, M. W. Lee, G. J. Wang, *Electrochem. Commun.* **2010**, *12*, 1158.
[19] K. G. Deepa, J. Nagaraju, *Mater. Sci. Semicond. Process.* **2014**, *27*, 649.
[20] S. P. Luo, H. P. Shen, W. Hu, Z. B. Yao, J. B. Li, D. Oron, N. Wang, H. Lin, *RSC Adv.* **2016**, *6*, 21156.
[21] J. J. Peng, Y. N. Chen, X. F. Zhang, A. G. Dong, Z. Q. Liang, *Adv. Sci.* **2016**, *3*, 1500432.
[22] C. H. M. Chuang, P. R. Brown, V. Bulović, M. G. Bawendi, *Nat. Mater.* **2014**, *13*, 796.
[23] Z. J. Ning, X. W. Gong, R. Comin, G. Walters, F. J. Fan, O. Voznyy, E. Yassitepe, A. Buin, S. Hoogland, E. H. Sargent, *Nature* **2015**, *523*, 324.
[24] G. Seo, J. Seo, S. Ryu, W. P. Yin, T. K. Ahn, S. I. Seok, *J. Phys. Chem. Lett.* **2014**, *5*, 2015.
[25] R. Lindblad, D. Q. Bi, B. W. Park, J. Oscarsson, M. Gorgoi, H. Siegbahn, M. Odelius, E. M. J. Johansson, H. Rensmo, *J. Phys. Chem. Lett.* **2014**, *5*, 648.
[26] F. Giordano, A. Abate, J. P. C. Baena, M. Saliba, T. Matsui, S. H. Im, S. M. Zakeeruddin, M. K. Nazeeruddin, A. Hagfeldt, M. Grätzel, *Nat. Commun.* **2016**, *7*, 10379.
[27] X. Li, D. Q. Bi, C. Y. Yi, J. D. Décoppet, J. S. Luo, S. M. Zakeeruddin, A. Hagfeldt, M. Grätzel, *Science* **2016**, *353*, 58.
[28] R. H. Chen, J. Cao, Y. Wu, X. J. Jing, B. H. Wu, N. F. Zheng, *Adv. Mater. Interfaces* **2017**, *4*, 1700897.
[29] Q. F. Dong, Y. B. Yuan, Y. C. Shao, Y. J. Fang, Q. Wang, J. S. Huang, *Energy Environ. Sci.* **2015**, *8*, 2464.
[30] Y. H. Deng, E. Peng, Y. C. Shao, Z. G. Xiao, Q. F. Dong, J. S. Huang, *Energy Environ. Sci.* **2015**, *8*, 1544.
[31] J. Burschka, N. Pellet, S. J. Moon, R. Humphry-Baker, P. Gao, M. K. Nazeeruddin, M. Grätzel, *Nature* **2013**, *499*, 316.
[32] M. D. Ye, C. F. He, J. Locozzia, X. Q. Liu, X. Cui, X. T. Meng, M. Rager, X. D. Hong, X. Y. Liu, Z. Q. Lin, *J. Phys. D: Appl. Phys.* **2017**, *50*, 373002.
[33] A. M. Smith, A. M. Mohs, S. M. Nie, *Nat. Nanotechnol.* **2009**, *4*, 56.
[34] S. P. Luo, M. Kazes, H. Lin, D. Oron, *J. Phys. Chem. C* **2017**, *121*, 11136.
[35] C. G. Wu, C. H. Chiang, Z. L. Tseng, M. K. Nazeeruddin, A. Hagfeldt, M. Grätzel, *Energy Environ. Sci.* **2015**, *8*, 2725.
[36] J. H. Im, I. H. Jang, N. Pellet, M. Grätzel, N. G. Park, *Nat. Nanotechnol.* **2014**, *9*, 927.
[37] Y. Zhang, X. H. Zhuang, K. Zhou, C. Cai, Z. Y. Hu, J. Zhang, Y. J. Zhu, *Org. Electron.* **2018**, *52*, 159.
[38] D. Chao, Y. H. Zhang, F. Liu, N. Nakazawa, Q. X. Huang, S. Z. Hayase, Y. Ogomi, T. Toyoda, R. X. Wang, Q. Shen, *ACS Appl. Mater. Interfaces* **2017**, https://doi.org/10.1021/acsami.7b06552.
[39] Z. G. Xiao, Q. F. Dong, C. Bi, Y. C. Shao, Y. B. Yuan, J. S. Huang, *Adv. Mater.* **2014**, *26*, 6503.
[40] Q. Luo, H. Ma, Y. Zhang, X. W. Yin, Z. B. Yao, N. Wang, J. B. Li, S. S. Fan, K. L. Jiang, H. Lin, *J. Mater. Chem. A* **2016**, *4*, 5569.
[41] A. Ummadisingu, L. Steier, J. Y. Seo, T. Matsui, A. Abate, W. R. Tress, M. Grätzel, *Nature* **2017**, *545*, 208.
[42] M. He, B. Li, X. Cui, B.B. Jiang, Y. J. He, Y. H. Chen, D. O'Neil, P. Szymanski, M. A. El-Sayed, J. S. Huang, Z. Q. Lin, *Nat. Commun.* **2017**, *8*, 16045.
[43] M. D. Xiao, F. Z. Huang, W. C. Huang, Y. Dkhissi, Y. Zhu, J. Etheridge, A. Gray-Weale, U. Bach, Y. B. Cheng, L. Spiccia, *Angew. Chem.* **2014**, *126*, 10056.
[44] B. V. Crist, *Handbook of Monochromatic XPS Spectra: The Elements of Native Oxides*, Wiley, Chichester, UK **1999**.
[45] S. E. Shaheen, C. J. Brabec, N. S. Sariciftci, *Appl. Phys. Lett.* **2001**, *78*, 841.
[46] H. Choi, S. J. Ko, T. Kim, P. O. Morin, B. Walker, B. H. Lee, M. Leclerc, J. Y. Kim, A. J. Heeger, *Adv. Mater.* **2015**, *27*, 3318.
[47] I. Moreels, Y. Justo, B. D. Geyter, K. Haustraete, J. C. Martins, Z. Hens, *ACS Nano* **2011**, *5*, 2004.